Chapter 6 ***Magnetic Properties of Dy Doped α-MnO_2 Nanorods***

6.1 Introduction

In previous chapter, we have demonstrated the effect of doping of dysprosium on α-MnO_2 nanorods and its effect on structural and electrochemical properties. We observed that 15% of Dy doped in α-MnO_2 nanorods possess high specific capacitance and can be used as an electrode in supercapacitors. In addition to its electrochemical characteristics, the magnetic properties are also interesting to study in these samples as there are rare report on the magnetic properties of rare earth doped α-MnO_2. Therefore, in this chapter, we have explained the evolution of magnetic properties of bare and 15 mol % Dy-doped MnO_2 nanorods synthesised using simple one step hydrothermal process. As structural modifications are already explained in the previous chapter, here the oxidation states are determined by X-ray photoelectron spectroscopy and illustrated in section 6.2. Magnetic properties are examined using temperature dependent magnetization, field dependent magnetization and remanant magnetization, as discussed in section 6.3. We observe a decrease in Neel temperature with an increase in Curie-Weiss temperature after doping Dy in α-MnO_2 nanorods indicating strong antiferromagnetic interaction. We measure exchange bias and training effect and have discussed on the basis of phenomenological models. The variation in exchange bias of both samples has been explained on the basis of core shell model and concluded in section 6.4.

6.2 X-ray Photoelectron Spectroscopy

Figure 6.1 depicts room temperature XPS spectrum of α-MnO_2 and α-MnO_2: Dy (Mn 2p and O 1s) fitted with Gaussian-Lorentz peak using software XPS peak 4.1 with straight background. All the peaks are calibrated with respect to the carbon 1s peak at 284.8 eV. Figure 6.1.1 (a) and (b) depicts Mn spectrum having two strong peaks attributed to Mn $2p_{3/2}$ and Mn $2p_{1/2}$ centred at 642.7 eV and 654.32 eV for α-MnO_2 and at 641.0 eV and 652.65 eV for α-MnO_2:Dy which are in good agreement with those of the standard MnO_2 [203][151]. Peak shift towards lower binding energy is ascribed to large Mn-O-Mn bond length leads to change in oxidation state of Mn after doping Dy. Further, deconvolution of Mn$2p_{3/2}$ peak reveal the oxidation state of Mn corresponds to +3 and +4 in α-MnO_2, in α-MnO_2: Dy Mn$2p_{3/2}$ peak is deconvoluted and belongs to +3 and +4 oxidation states, respectively. Due to shift in energy from 654.32 eV to 652.65 eV in α-MnO_2: Dy indicates that the oxidation state of Mn changes from +4 to +3. The ratio of Mn^{3+}/Mn^{4+} in α-MnO_2 and α-MnO_2: Dy is estimated to be 0.68 and 3.52. The XPS spectrum of Dy 4d shown in figure 6.1.2, deconvoluted into two peaks at 152.7 eV and 155.38 eV confirms the +3 oxidation state. Figure 6.1.3 shows the spectrum of O 1s deconvoluted into two peaks observed at 528.40 eV and 531.8 eV represents the presence of lattice oxygen (O_a) (Mn-O-Mn) and surface oxygen (O_b), respectively. The area ratio of O_b and O_a in α-MnO_2 and α-MnO_2: Dy is found to be 1.050 and 1.575, respectively. One may note that concentration of oxygen vacancies increases after doping Dy which corroborates with increase in Mn^{3+} as obtained from Mn2p spectrum. Therefore, it is interesting to note that both specific capacitance and magnetic moment increases with doping Dy. While Dy doping inhibits the growth of nanorods and show high surface area and high capacitance, high magnetic

moment is accompanied with large concentration of Mn^{3+} due to Dy doping and the magnetic moment of Dy itself.

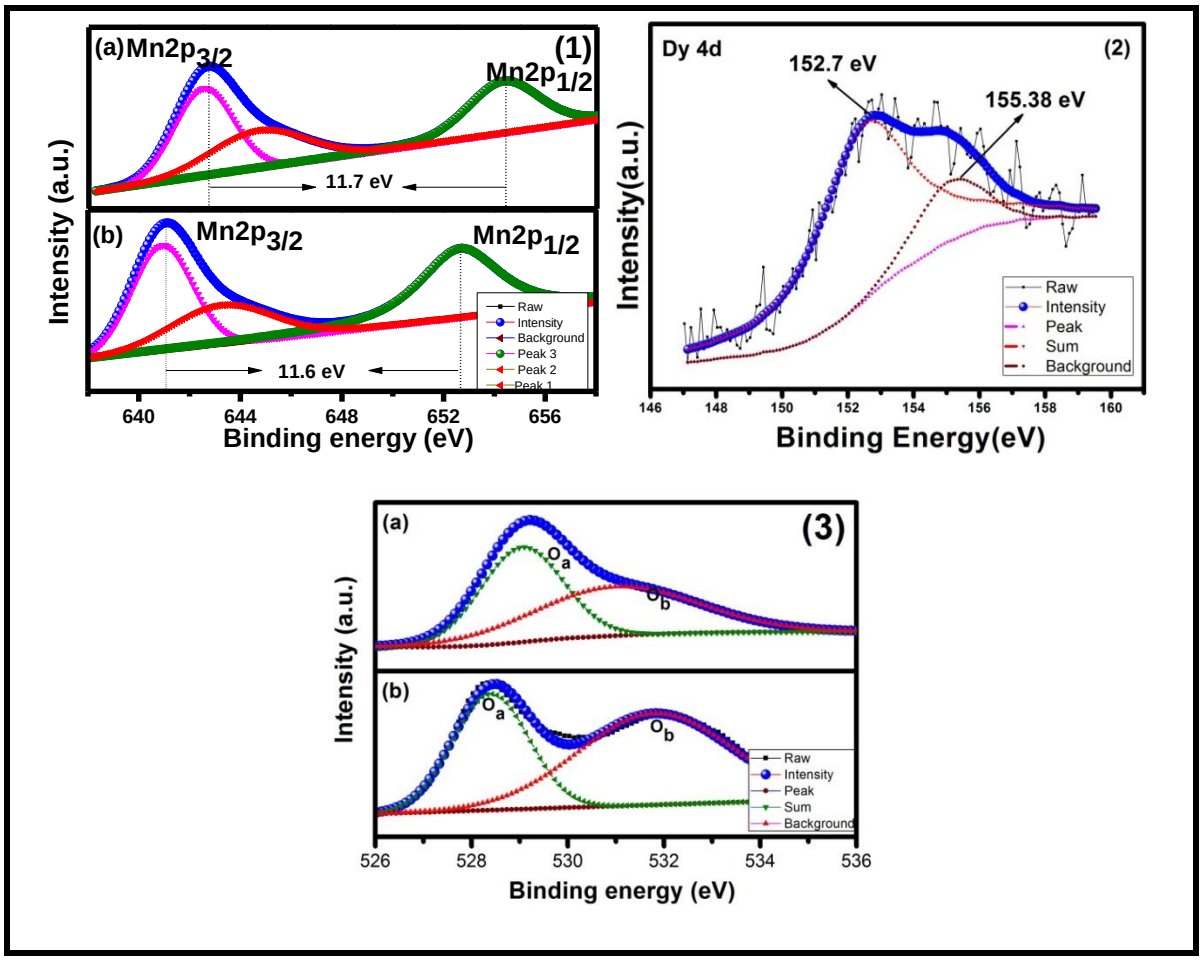

Figure 6.1: *(1) X-ray photoelectron spectroscopy for Mn 2p in (a) α-MnO_2 (b) α-MnO_2:Dy, (2) Dy 4d in α-MnO_2 and (3) for O1s in (a) α-MnO_2 and (b) α-MnO_2:Dy nanorods.*

6.3 Magnetic Properties

To explain magnetic properties of bare and 15 mol % Dy-doped MnO_2 nanorods the temperature dependent magnetization, magnetic field dependent magnetization, remanant magnetization measurement and training effect are carried out and are discussed in section 6.3.1, 6.3.2, 6.3.3 and 6.3.4, respectively.

6.3.1 Temperature Dependent Magnetization

Temperature dependent dc magnetization has been measured after zero-field-cooling (ZFC) and field-cooling (FC) protocols from 2K to 300 K at an external magnetic field of 100 Oe, as shown in figure 6.2. For ZFC mode, the sample is cooled down from 300 K to 2 K without applying magnetic field whereas, for FC mode, the sample is cooled in the presence of 100 Oe. One may note that, for α-MnO_2, decreasing the temperature from 300 K, M_{ZFC} and M_{FC} curves show a clear bifurcation below T_{irr} ~50 K followed by a peak at 18 k which is the Neel temperature, T_N. After doping Dy in α-MnO_2, a drastic change in M_{ZFC}/M_{FC} behaviour is depicted in figure 6.2. The peak corresponds to Neel temperature, T_N becomes broad and shift towards lower temperature at 11 K which may be due to reduced size of nanorods and/or effect of Dy incorporation. Similar decrease in T_N by 10 K has been observed in $MnO_{2-\delta}$ nanowire microspheres than that of bulk MnO_2 (*Yang et al*) [53]. Further, decreasing the temperature down to T_N, a clear anomaly is observed at 4 K in α-MnO_2: Dy in both FC and ZFC magnetization which is absent in α-MnO_2 (Figure 6.2). The above magnetic anomaly represents the Dy- Dy antiferromagnetic interaction [204]. Further, we have fitted inverse susceptibility in paramagnetic region i.e from 150 to 300 K with Curie Weiss law, $1/\chi = (T-\theta_{cw})/C$, where C is the Curie constant and θ_{cw} is the Cure-Weiss temperature as shown in figure 6.3 (a) and (b). From fitted results, θ_{cw} is found to be

-234 K and -293 K for bare and α-MnO_2: Dy, respectively. More negative value of θ_{cw} in α-MnO_2: Dy indicates a strong antiferromagnetic interaction than that of α-MnO_2. The effective paramagnetic moment for corresponding materials has been determined using following equation

$$\mu_{eff} = \sqrt{[3Ck_{\beta} / (N_A \mu_B^2)]} \qquad [6.1]$$

where k_β is Boltzmann's constant and N_A is Avogadro's number [205]. The experimental μ_{eff} obtained for bare and MnO_2: Dy are 4.62μ_B and 5.95μ_B respectively, which is larger than the effective moment of Mn^{4+} ion (3.87μ_B). The large magnetic moment in both samples are due to the presence of Mn^{3+} ions which is having higher magnetic moment (4.90 μ_B) in high spin state than that of Mn^{4+}.

The high magnetic moment in α-MnO_2: Dy compared to bare one is attributed to the presence of Dy^{3+} which is having μ_{eff} of 10.48 μ_B and large number of Mn^{3+} ions after doping Dy. If this is case then, we expect more oxygen vacancies in α-MnO_2: Dy nanorods. Although, α-MnO_2 is antiferromagnetic in nature, due to nanosize of the rods, one may expect uncompensated spins at the surface of nanorods and may exhibits ferrimagnetic behaviour. We have fitted reciprocal susceptibility (χ^{-1}) of paramagnetic range with temperature with the following function:

$$\chi^{-1} = \frac{T}{C} + \frac{1}{\chi_0} - \frac{b}{T-\theta} \qquad [6.2]$$

The above function consists of Curie-Weiss (ferrimagnetic) and a Curie (paramagnetic) term [192]. Figure 6.3 (a) and (b) show the fitting of experimental data with above equation

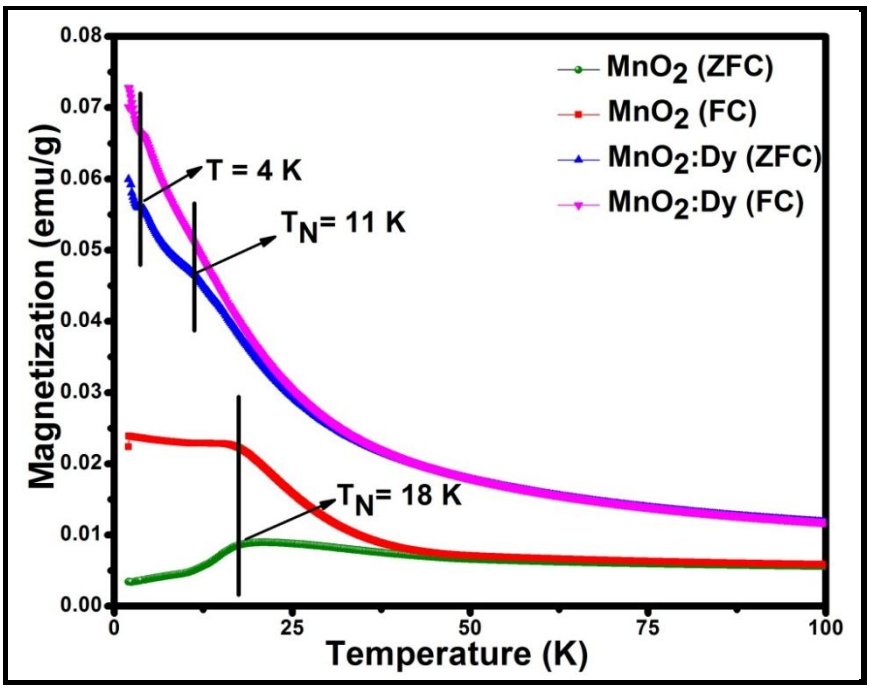

Figure 6.2: *Temperature dependent magnetization of (a) α-MnO_2 and α-MnO_2:Dy under ZFC and FC.*

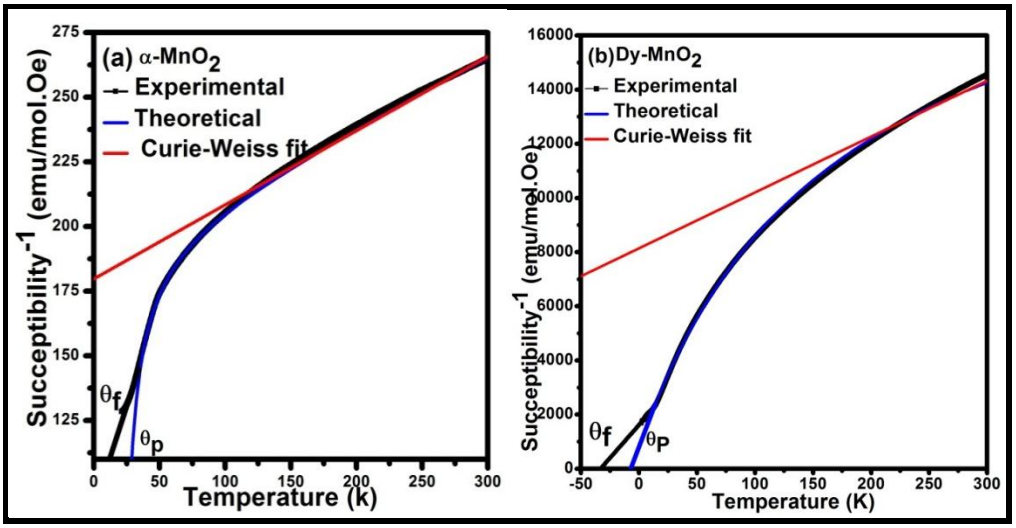

Figure 6.3: *The inverse susceptibility,1/χ Vs. T data in paramagnetic region is fitted with the equation $\chi^{-1} = T/C + 1/\chi_o - b/(T-\theta)$ for (a) α-MnO_2 and (b) α-MnO_2:Dy measured at an external applied field of 100 Oe.*

except near the Curie point. Extrapolation of the experimental data intersects the temperature axis at θ_f, called as ferrimagnetic Curie point while data fitted with the equation cut at θp, called paramagnetic Curie point. From figure, one may note that there is a clear disagreement between the values of θ. However, the difference in θp and θ_f in α-MnO_2 is found to be 16K. θp and θ_f are positive in α-MnO_2 whereas it is negative after doping Dy. Thus, one may confirm that α-MnO_2: Dy shows strong antiferromagnetic behaviour.

Confirming the presence of Mn^{3+} in addition to Mn^{4+} in these samples, we have further determined the fraction of the Mn^{3+} ions using following equation [162]:

$$\mu_{eff}^2 = (1 - y)\,[\mu_{eff}(Mn^{4+})]^2 + y\,[\mu_{eff}(Mn^{3+})]^2 \qquad [6.3]$$

Where, y denotes the concentration of Mn^{3+}. As a result, we obtain y = 0.704 and 2.26 for α-MnO_2 and α-MnO_2: Dy nanorods, respectively. According to electrostatic charge neutrality, extra Mn^{3+} ions are present in the matrix confirm the presence of oxygen vacancies. Two Mn^{3+} ions will create an oxygen vacancy with increasing Mn^{3+}/ Mn^{4+} ratio. One may find actual composition of α-MnO_2 and α-MnO_2: Dy should be $MnO_{1.65}$ and $MnO_{0.87}$. This clearly indicates the role of oxygen vacancy, responsible for high effective magnetic moment which further increases after doping Dy.

6.3.2 Field Dependent Magnetization

Figure 6.4 depicts the magnetization verses external magnetic field for α-MnO_2 and α-MnO_2: Dy nanorods at different temperature (2K, 15K and 30K) under ZFC condition in the range of ±70 kOe. Linear increase in magnetization with the magnetic field confirms the paramagnetic behaviour of both samples. No loop at 15 K shows the antiferromagnetic

nature while at 2K both sample exhibits a weak hysteresis loop with a non-saturation magnetization which indicates weak ferromagnetic ordering at low temperatures. Field-dependent magnetization under ZFC and FC condition at 2K with application of 10 kOe for α-MnO_2 and α-MnO_2: Dy depicted in figure 6.5 (a) reveals non-saturated hysteresis loops. Hysteresis loops observed in both samples indicate a deviation from antiferromagnetic behaviour. We observe coercive field of 2 kOe and 1 kOe for α-MnO_2 and α-MnO_2: Dy, respectively as shown in the upper inset of figure 6.5 (a). Thus, it provides an evidence for mixed state of antiferromagnetic and uncompensated surface spins. Decrease in coercivity after doping attributes to increasing antiferromagnetic phase fraction. At higher applied field, although magnetization linearly increases without showing any saturation in both cases, maximum magnetization (M_{max}) is found to be enhanced by three times in α-MnO_2: Dy than that of α-MnO_2 due to presence of Dy. Hysteresis loop measured under field cooling (FC) condition shifts towards negative field indicating the existence of exchange bias (EB) phenomenon in both samples. The exchange bias field (H_{EB}) and coercive field (H_C) are determined by using the following equations:

$$H_{EB} = (Hc_1 + Hc_2) / 2 \text{ and} \qquad [6.4]$$

$$H_C = \left| Hc_1 - Hc_2 \right| / 2 \qquad [6.5]$$

Where, Hc_1 and Hc_2 are the left and right coercive fields, respectively [1][206]. At the cooling field of 10 kOe, we obtain an H_{EB} of 290 Oe and 105 Oe for α-MnO_2 and α-MnO_2: Dy, respectively. To further confirm the existence of exchange bias, field dependent magnetization measurements have been carried out at different cooling field of 20 and 30 kOe. Lower inset of figure 6.5(b) clearly demonstrates that exchange bias increases with an

increase in the cooling field. H_{EB} increases from 565 Oe to 160 Oe by increasing field from 10 kOe to 30 kOe for α-MnO_2 and α-MnO_2: Dy, respectively. Significant increase in EB in α-MnO_2 can be explained from core shell structure of nanorods obtained in these compounds as depicted in Figure 6.6. While core of the nanorods are constituted by antiferromagnetic frozen spins and are irreversible under field, the spins at the surface are rotatable and reversible easily with field. The interaction at the interface results in very different magnetic behavior as observed in these two different sizes of nanorods.

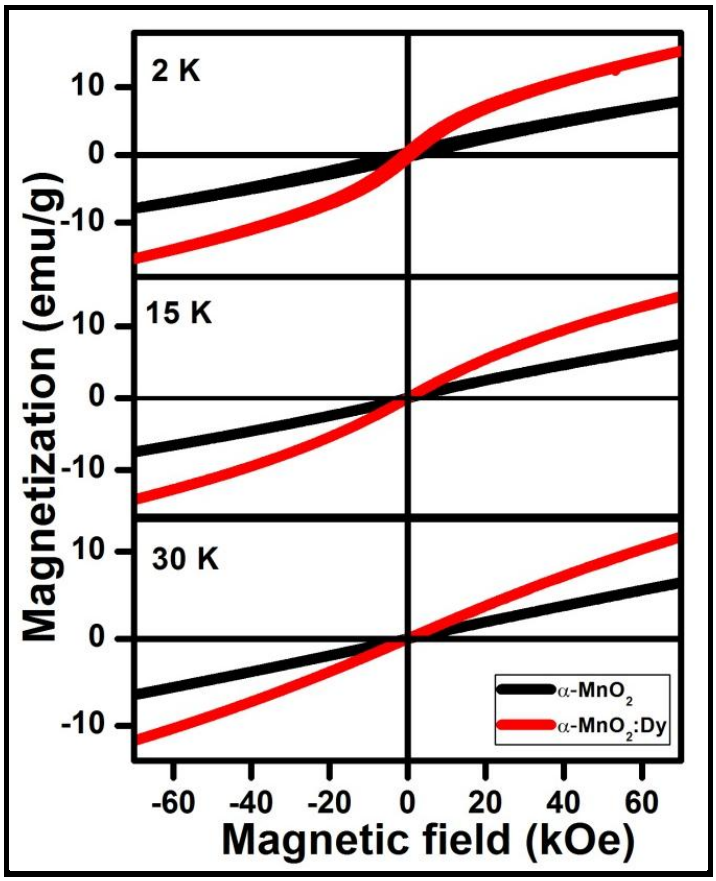

Figure 6.4: *Field dependent magnetization M(H) for ZFC at 2K, 15K and 30K of α-MnO_2 and α- MnO_2:Dy nanorods.*

Appearance of exchange bias is one of the outcomes of the interaction between these two different kinds of spins. Rapid increase in exchange bias in α-MnO_2 is attributed to large number of antiferromagnetic spins at the core compared to that of rotatable spins which provides an extra pinning force to maintain the magnetization force in the direction of cooling field and results in increase in exchange bias field. On the contrary, the decrease in EB field in α-MnO_2: Dy is attributed to more rotatable spins at the surface compared to that of AFM spins of the core. This could possible due to the reduction of size from 40 nm in α-MnO_2 to 20 nm in α-MnO_2: Dy. Smaller is the size, higher is the surface to volume ratio and hence higher is the contribution of rotatable spins at the surface of nanorods in Dy doped α-MnO_2.

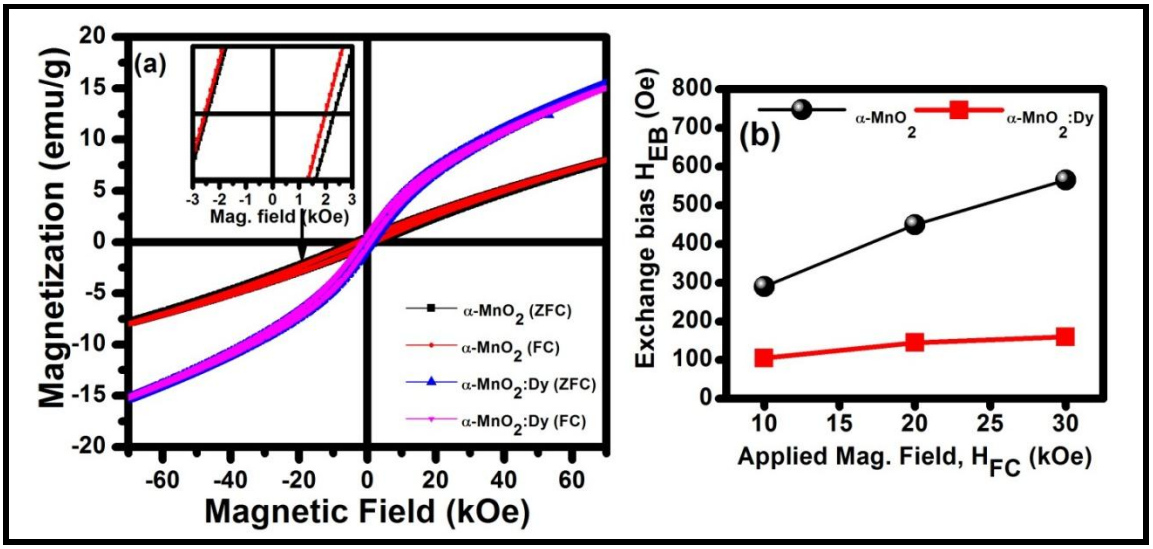

Figure 6.5: *(a) Field dependent magnetization M(H) for FC under the field of 10 kOe at 2K of α-MnO_2 and α-MnO_2:Dy nanorods. Upper inset shows the corresponding coercivity at positive field of α-MnO_2. (b) Shows the variation of exchange bias with cooling field for both samples.*

6.3.3 Remanant Magnetization Measurement

Further the competition between these two kinds of spins results in the three times reduction in M_{max} and spin-glass (SG) phase, in α-MnO_2 which is absent in α-MnO_2:Dy which has been confirmed from time dependent thermoremanent remnant magnetization, [M(t)] as shown in figure 6.7. For this measurement, the sample has been cooled down from 300 to 2 K in the presence of an external magnetic field of 100 Oe. After the removal of magnetic field, magnetization decay has been recorded as a function of time. We observe that for α-MnO_2, remnant magnetization relaxes very slowly giving an evidence of the existence of SG behaviour. However, a rapid decrease in magnetization is observed in case of α-MnO_2:Dy. Resultant plot is fitted using stretched exponential function given in equation [184][207]:

$$M(t) = Mo + Mr \exp[-(t/\tau)^{1-n}] \qquad [6.6]$$

where M_o is the intrinsic static magnetization component, M_r is the glassy component, τ is the stretched exponential time and n is the stretched exponential exponent. For bare α-MnO_2, resultant plot is well fitted with eq. (6.6) with a value of τ and n extracted for SG ordering as 5,637 sec and 0.746, respectively. Thus, resulting magnetization behaviour favours the existence of spin glass phase in the system. Above T_{irr}, the spins are independent, which on decreasing temperature below T_{irr} form small correlated regions called clusters or domains. These clusters slowly fluctuate below T_{irr} resulting a well-defined frozen ground state of the system. Similar slow relaxation of spins below freezing temperature also reported by *Le et al.* approaches a glassy ground state [153]. However, for α-MnO_2: Dy, sudden fall in magnetization curve demonstrates no evidence of the existence of remnant magnetization or a SG state (inset of figure 6.7).

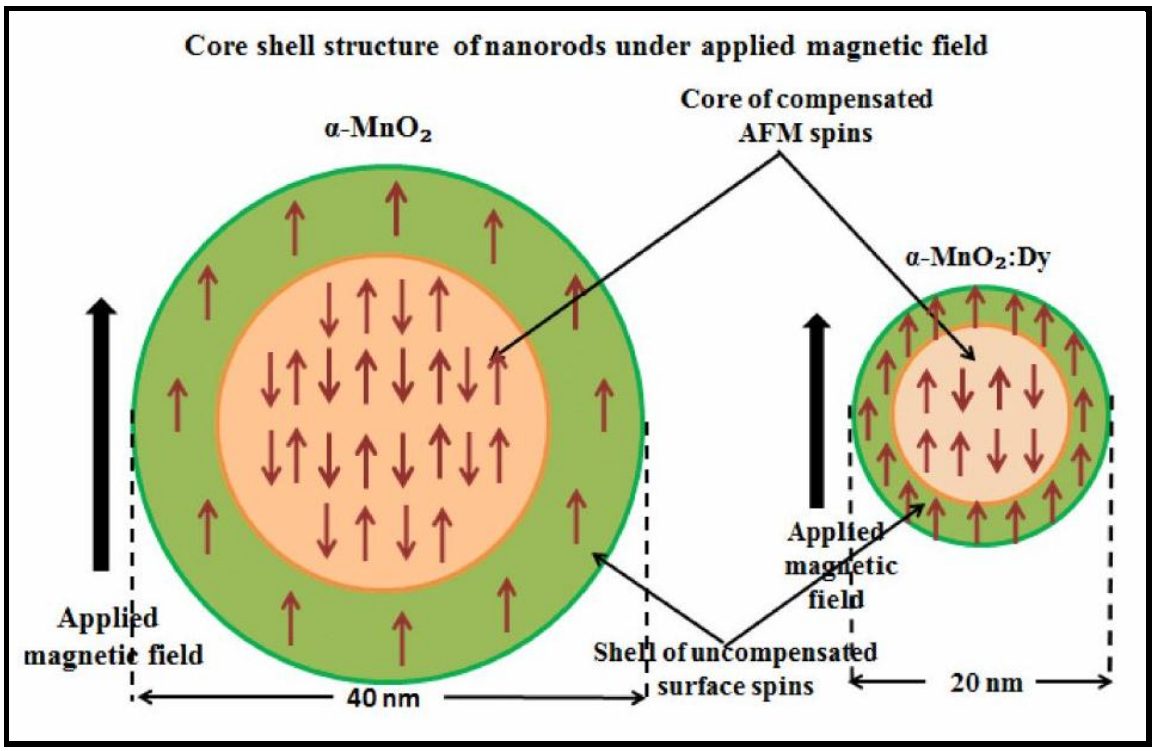

Figure 6.6: *Schematic of core shell model of α-MnO_2 and α-MnO_2:Dy nanorods having diameter 40 and 20 nm, respectively. The arrows indicate the magnetic state of the spins after initial magnetization.*

6.3.4 Training Effect

Essential characteristic of the exchange bias (EB) phenomena is so-called training effect (TE), which manifests the reduction in H_{EB} through several consecutive hysteresis cycles at fixed temperature. In order to understand the exchange bias phenomenon under FC condition, training effect has been performed for 5 consecutive cycles after applying cooling filed of 30 kOe with H_{max} = ±70 kOe. Training effect can be well explained in two steps. The first step is the steep reduction of H_{EB} in the first two loops followed by a

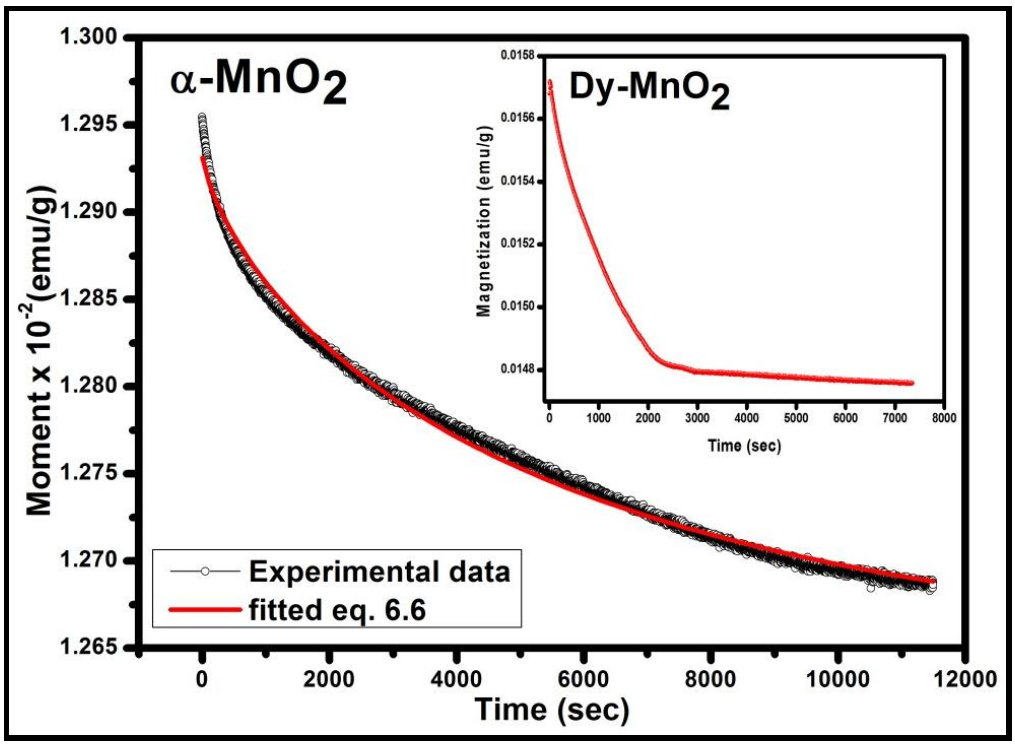

Figure 6.7: *Variation of thermoremanent remnant magnetization [M(t)] at 2K for α-MnO_2 and α-MnO_2:Dy (in inset) nanorods.*

gradual decrease in H_{EB} for subsequent loops. This is a conventional training mechanism related to uncompensated frozen spins which cause a larger reduction in exchange bias after the first cycle. The later type of training effect is due to the reconfiguration of spins or domain state of the AFM during consecutive cycles. A gradual decrease in exchange bias has been observed with increasing number of cycles are tabulated in table 6.1. Moreover, the changes are most pronounced at the left branch of the loop, shown in figure 6.8 (a), while the right branch evolves slightly. The variation of coercive fields in negative and positive field axis with number of loops are shown in figure 6.8 (b). It clearly shows that there is a rapid decrease in EB after first cycle in α-MnO_2 as compared to α-MnO_2: Dy and monotonously decreases for successive cycles. The relative decrease in exchange bias with

increasing number of loops is explained by determining the percentage of training effect using the following equation [208][209]:

$$\mathrm{TE}(\%) = \left(1 - \frac{\mathrm{H}_{\mathrm{EB}}^{1} - \mathrm{H}_{\mathrm{EB}}^{\mathrm{n}}}{\mathrm{H}_{\mathrm{EB}}^{1}}\right) \times 100(\%) \qquad [6.7]$$

Table 6.1: Numeric value of exchange bias field and percentage of training effect during each cycle for bare and Dy doped α-MnO_2.

No. of loops (n)	Bare MnO_2		Dy-MnO_2	
	H_{EB} = (Hc_1 + Hc_2) / 2	% of TE	H_{EB} = (Hc_1 + Hc_2) / 2	% of TE
1	565	100	140	100
2	265	46.9	85	60.7
3	255	45.1	70.5	50.3
4	230	40.7	60	42.8
5	220	38.9	56.5	40.7

where $\mathrm{H}_{\mathrm{EB}}^{\mathrm{n}}$ is the exchange bias field of nth cycle. From table 6.1, we observe that percentage of decrease in exchange bias after first loop of training effect is 53% and 39% for α-MnO_2 and α-MnO_2: Dy respectively, which is larger than the subsequent loops. At the end of 5 cycles the training effect for both samples is decreased by 40.7 % and 42.8%, respectively. Due to the presence of less number of frozen spins in α-MnO_2: Dy, EB after 5 loops is found to be significantly less than that of α-MnO_2. Variation of H_{EB} with number of loops (n) can be fitted by using following Power law equation:

$$\mu_o H_{EB}(n) - \mu_o H_{EB}^{e} = \frac{K}{\sqrt{n}} \text{ (for, } n \geq 2) \qquad [6.8]$$

where n is the number of loops traversed, k is a system dependent constant, and H_{EB}^{e} is the exchange bias field in the limit of infinite loops [210]. Figure 6.9 depicts the fitted experimental data of equation 6.8 for both samples. Estimated values of k and H_{EB}^{e} for α-MnO_2 and α-MnO_2: Dy are 623, 94.5 Oe and 161, 23 Oe respectively. Training effect can be well explained in two steps. First step is the steep reduction of H_{EB} in first two loops followed by a gradual decrease in H_{EB} for subsequent loops. This is a conventional training mechanism related to uncompensated frozen spins which cause larger reduction in exchange bias after first cycle. The later type of training effect is due to the reconfiguration of the spins or domain state of the AFM during consecutive cycles [211]. Fitting H_{EB} with above equation, the steep increase in H_{EB} for n=1 is not fitted well for α-MnO_2. However, in α-MnO_2: Dy, for n=1 to 5 cycles, the power law equation is fitted well with experimental H_{EB} values. A less significant decrease of exchange bias between first and second hysteresis loop in α-MnO_2: Dy suggests that rotatable spins dominates and no rearrangement of spins takes place during continuous magnetization cycle. Breakdown of power law for n = 1 in α-MnO_2 suggests that single exponential function could not describe the phenomenon completely. Therefore, training effect has been described using two different relaxation rates by using following double exponential equation:

$$H_{EB}(n) = H_{EB\infty} + A_f \exp(-n/P_f) + A_i \exp(-n/P_i) \qquad [6.9]$$

where, A_f and P_f are the parameters associated with frozen spins, A_i and P_i are corresponding to rotatable spin components at the interface. Dimension of parameter A is

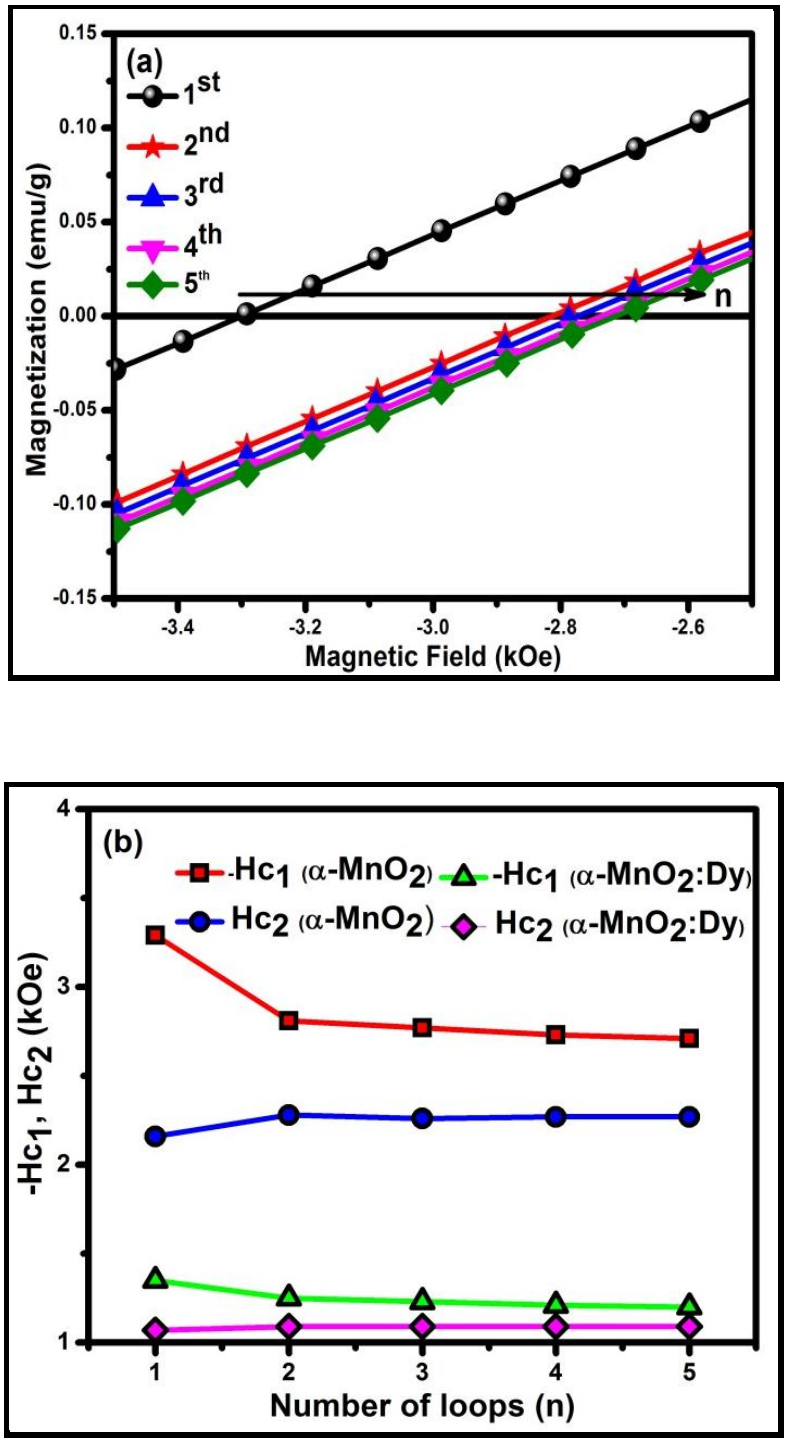

Figure 6.8: *(a) Enlarge view of five hysteresis loops to reveal the shift of the loop with increasing loop number for α-MnO_2, (b) Variation of coercive fields Hc_1 and Hc_2 with number of recurrent hysteresis loops n.*

the dimension of magnetic field (Oersted) while parameter P is dimensionless and resembles a relaxation time, although the continuous variable (n) is replaced by discrete loop number [212]. The contributions of rotatable and frozen AFM spins at the interface are comparable at the primary stage of the training effect but the frozen spins relax much slower with respect to rotatable ones. Experimental values are well fitted with above equation for both the samples with fitting parameters as listed in table 6.2 (figure 6.9).

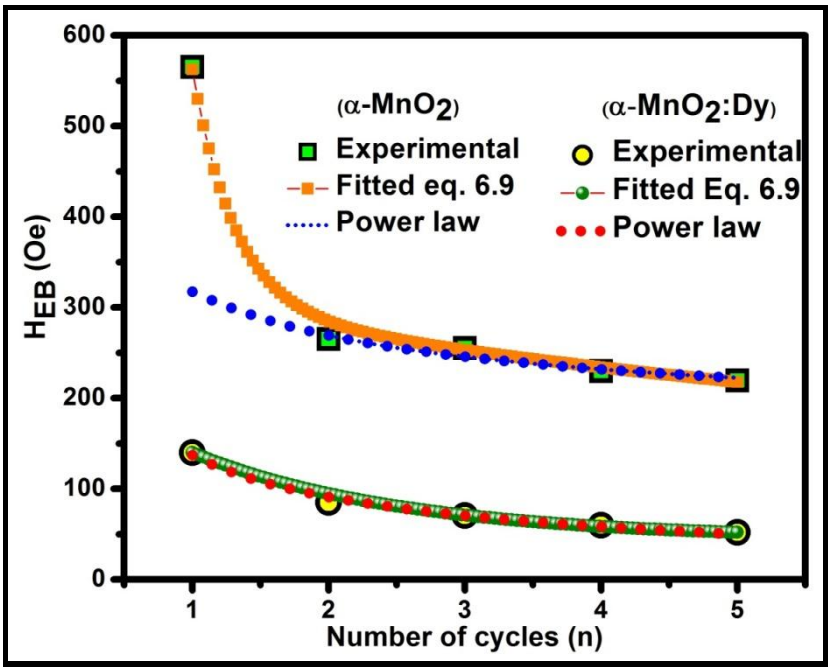

Figure 6.9: *symbols represent the experimental data for H_{EB} versus loop index number (n). Dotted line corresponds to a fit with a power law for n≥2 , while solid line illustrates the best fit with equation 6.9.*

For α-MnO_2, huge difference between A_f , A_i and P_f , P_i indicate that frozen spins are dominate over rotatable spins. The relative rate of relaxation of frozen and rotatable spins, P_f / P_i, measures the difference in relaxation of both the components which is found to be

smaller for α-MnO_2 [213]. Hence, frozen spins are unstable during each magnetization reversal and results a decrease in H_{EB} in α-MnO_2.

Table 6.2: Values of the expression 6.9 fitting parameters approximating experimental data for training effect.

Sample	**$H_{EB\infty}$ (Oe)**	**A_f (Oe)**	**P_f**	**A_i (Oe)**	**P_i**
MnO_2	192.29	38526.54	0.19	209.43	2.42
Dy-MnO_2	56.25	791.19	0.25	164.74	1.15

6.4 Conclusion

In the present work, magnetic properties α-MnO_2 and α-MnO_2:Dy nanorods were explored. Neel temperature of α-MnO_2 was found to be 18 K less than that of bulk α-MnO_2 (T_N = 24.5 K) and further decreased to 11 K after doping Dy with an increasing antiferromagnetic interaction. The existence of exchange bias was found in both samples by observing a clear shift in field cooled M-H loops. For α-MnO_2, large H_{EB} of 565 Oe was obtained which decreased to 140 Oe after doping Dy at the cooling field of 30 kOe. Such variation of exchange bias field was understood on the basis of core shell structure which consists of frozen and rotatable spins in the core and surface of nanorods respectively. The competition between them resulted in spin-glass behaviour and high exchange bias in α-MnO_2. Further, we discussed the mechanism behind the variation in exchange bias with number of cycles of hysteris loops using power law and double exponential equation.